

Continued development of the one-way Euler equations: application to jets

Aaron Towne* and Tim Colonius†

California Institute of Technology, Pasadena, CA, 91125, USA

An efficient method for calculating linearized disturbances to shear flows that accurately captures their acoustic radiation was recently introduced (Towne & Colonius, *AIAA Paper 2013-2171*, 2013). The linearized Euler equations are modified such that all upstream propagating acoustic modes are removed from the operator. The resulting equations, called one-way Euler equations, can be stably and efficiently solved in the frequency domain as a spatial initial value problem in which initial perturbations are specified at the flow inlet and propagated downstream by integration of the equations. In this paper, we continue the development of this method with the aim of using it to model wavepackets and their acoustic radiation in turbulent jets. Before turning attention to jets, two dimensional mixing layer noise results computed using the one-way Euler equations are shown to be in excellent agreement with a direct solution of the full Euler equations. The one-way Euler operator is then shown to accurately represent all downstream modes that exist in supersonic and subsonic parallel jets, while properly eliminating the upstream acoustic modes. Finally, the method is applied to a turbulent Mach 0.5 jet mean flow obtained from experimental measurements. The near-field one-way Euler results are similar to those obtained using a previous spatial marching technique called the parabolized stability equations. However, the one-way Euler solutions also include the acoustic fields. With further development, the results suggest that the one-way Euler equation could be used to obtain improved accuracy over the parabolized stability equations as a low-order jet noise model.

I. Introduction

A wide range of experimental and numerical investigations have identified large-scale coherent structures in turbulent jets.¹ These structures take the form of advecting wavepackets with nearly constant wavelength and exhibit coherence over distances exceeding turbulent length scales. Although large-scale wavepackets constitute a modest portion of the total turbulent flow energy, their high spatiotemporal coherence makes them acoustically efficient relative to uncorrelated turbulent fluctuations. In particular, wavepackets are correlated with acoustic radiation to downstream angles, where sound is most intense.²

The process by which supersonically convected wavepackets produce sound is well known and corresponds to a wavy-wall-like mechanism leading to Mach wave radiation.³ Constant amplitude subsonically convected waves, on the other hand, do not produce sound. However, when such a wave undergoes a change in amplitude, its wavenumber is no longer discrete and some of its energy becomes acoustically matched to propagating solutions of the wave equation.^{1,3} It is therefore the growth and decay of wavepackets that contributes to sound production in subsonic jets.

Suzuki & Colonius⁴ showed that these wavepackets can be quantitatively identified as linear instability modes of the turbulent mean flow. This suggests that reasonable low-cost jet noise models could be obtained through accurate calculation of linear modal solutions.

By assuming that the mean jet is locally parallel, Michalke⁵ and Mattingly & Chang⁶ applied classical linear stability theory to experimentally measured velocity profiles to compute local eigenvalues and found good agreement with experimental growth rate and wavenumber estimates. However, the local nature of such methods limits their ability to accurately capture nonparallel effects and the downstream growth and decay of the instability waves.

*Ph.D. student.

†Professor, AIAA Associate Fellow.

To address this shortcoming, a variety of weakly-nonparallel methods were developed based on the method of multiple scales^{7,8} and matched asymptotic expansion.³ These methods partially account for the slow divergence of the jet mean flow and deliver reasonable results, especially in the near-field. They are, however, mathematically intricate and must be appropriately modified to account for each new flow configuration considered.

A simpler, more robust approach for incorporating slow mean flow divergence is an *ad hoc* generalization of linear stability theory called the parabolized stability equations (PSE).⁹ PSE can partially capture non-parallel and nonlinear effects, and has been shown to accurately model many convectively unstable flows. In particular, our group has previously shown that linear PSE produces quantitatively accurate near-field wavepackets for both supersonic¹⁰ and subsonic¹¹ turbulent jets. For supersonic jets, the far-field noise is also well predicted by PSE.¹² On the other hand, PSE severely under-predicts the far-field noise for subsonic jets.¹³

PSE is a frequency-space spatial marching technique in the streamwise direction. Initial conditions are specified at the jet inlet and propagated downstream by integration of the PSE operator. Because of this one-way solution strategy, upstream propagating waves cannot be captured by PSE. Care must be taken to assure a stable downstream march. This is the case because, despite their name, the parabolized stability equations are not formally parabolic. The PSE operator contains remnants of upstream acoustic modes that constitute an elliptic effect in the frequency domain. These elliptic modes are a consequence of the inherent boundary value nature of the subsonic Euler equations. Specifically, decaying upstream acoustic modes are wrongly interpreted by the PSE operator as growing downstream modes, causing exponential instability in the march if they are not eliminated. The traditional PSE method attenuates these waves by using an implicit Euler axial discretization along with a restriction on the *minimum* step size. This has the effect of numerically damping the upstream acoustic modes such that they move inside the unit circle in the discrete spectral space. If a step size below the restriction is used, these modes again move outside of the unit circle and cause unbounded instability.¹⁴

An unintended consequence of the numerical damping used to eliminate the upstream acoustic modes is that PSE effectively damps or otherwise distorts all but a single mode of the Euler operator. For shear flows, the one mode that PSE faithfully tracks (which we call the primary PSE mode) is the Kelvin-Helmholtz mode. As a result, the desired downstream acoustic modes are poorly computed. The downstream acoustic modes in subsonic jets are more susceptible to this numerical damping than their counterparts in supersonic jets. The implicit Euler discretization applies damping in such a way that modes that are farther from the Kelvin-Helmholtz mode in the complex spectral plane are more seriously damaged. The lower phase velocity of the Kelvin-Helmholtz mode in subsonic jets increases the distance of this mode from the sonically propagating downstream acoustic modes, effectively increasing the damping of these modes compared to supersonic jets. Several alternative methods^{15,16} have been devised to remove the upstream acoustic mode from the PSE operator and reduce the minimum allowable step size, but each of these methods still has catastrophic effects on the downstream acoustic radiation, especially for subsonic flows.

Towne & Colonius¹⁷ recently introduced an alternative parabolization technique and applied it to the two dimensional Euler equations. The resulting equations, termed the one-way Euler equations (OWE), do not contain upstream acoustic modes and can be stably integrated in the downstream direction. Furthermore, the downstream acoustic modes are accurately retained, allowing far-field acoustic radiation to be properly captured.

In this paper, we extend the one-way Euler methodology with the aim of ultimately using it to model wavepackets and their acoustic radiation in turbulent subsonic jets. We begin in section II by deriving the one-way Euler equations in cylindrical coordinates. Section III contains two test problems that verify the convergence and accuracy of the method. In section IV, we first demonstrate the ability of the one-way Euler equations to accurately represent the various modal families that exist in supersonic and subsonic parallel jets. We then apply the method to a Mach 0.5 turbulent jet. Section V concludes the paper.

II. Method

In this section, we outline our method for parabolizing the Euler equations. We first derive the linearized Euler equations in cylindrical coordinates and manipulate them into a form convenient for parabolization. Then, assuming parallel flow, we derive exact one-way Euler equations. This formulation turns out to be computationally intractable in most cases, so we formulate an alternative approximate one-way equation

that converges to the exact one-way equation as the order of the approximation is increased. Then, we discuss the application of these methods to non-parallel flows and finally compare the computational cost of the one-way equations to other solution techniques.

II.A. The linearized Euler/Navier-Stokes equations

We begin with the compressible Navier-Stokes equations in cylindrical coordinates:

$$\frac{D\nu}{Dt} - \nu(\nabla \cdot u) = 0, \quad (1a)$$

$$\frac{Du_x}{Dt} + \nu \frac{\partial p}{\partial x} = \frac{1}{Re} \nu \nabla^2 u_x, \quad (1b)$$

$$\frac{Du_r}{Dt} - \frac{u_\theta^2}{r} + \nu \frac{\partial p}{\partial r} = \frac{1}{Re} \nu \left(\nabla^2 u_r - \frac{u_r}{r^2} - \frac{2}{r^2} \frac{\partial u_\theta}{\partial \theta} \right), \quad (1c)$$

$$\frac{Du_\theta}{Dt} + \frac{u_r u_\theta}{r} + \frac{\nu}{r} \frac{\partial p}{\partial \theta} = \frac{1}{Re} \nu \left(\nabla^2 u_\theta - \frac{u_\theta}{r^2} + \frac{2}{r^2} \frac{\partial u_r}{\partial \theta} \right), \quad (1d)$$

$$\frac{Dp}{Dt} + \gamma p (\nabla \cdot u) = \frac{\gamma}{Re Pr} (\nu \nabla^2 p + p \nabla^2 \nu), \quad (1e)$$

with

$$\frac{D}{Dt} = \frac{\partial}{\partial t} + u_x \frac{\partial}{\partial x} + u_r \frac{\partial}{\partial r} + \frac{u_\theta}{r} \frac{\partial}{\partial \theta},$$

$$\nabla^2 = \frac{\partial^2}{\partial x^2} + \frac{\partial^2}{\partial r^2} + \frac{1}{r} \frac{\partial}{\partial r} + \frac{1}{r^2} \frac{\partial^2}{\partial \theta^2},$$

and

$$\nabla \cdot u = \frac{\partial u_x}{\partial x} + \frac{\partial u_r}{\partial r} + \frac{u_r}{r} + \frac{1}{r} \frac{\partial u_\theta}{\partial \theta}.$$

We have chosen as independent variables specific volume ν , axial velocity u_x , radial velocity u_r , azimuthal velocity u_θ , and pressure p . All variables have been appropriately non-dimensionalized by an ambient sound speed c_∞ and density ρ_∞ and a problem dependent length-scale D (nozzle diameter for jet problems). The fluid is approximated as a perfect gas with specific heat ratio γ and constant Reynolds number Re and Prandtl number Pr . We have neglected viscous energy dissipation and assumed that the gradient of the dilatation is small.

We decompose the flow-field $q = \{\nu, u_x, u_y, u_\theta, p\}^T$ into a steady, axisymmetric baseflow and fluctuations about this baseflow:

$$q(x, r, \theta, t) = \bar{q}(x, r) + q'(x, r, \theta, t). \quad (2)$$

If non-linear products of fluctuations are neglected and the baseflow satisfies equation (1), then the fluctuations satisfy the linearized, two-dimensional, compressible Navier-Stokes equations:

$$\frac{\partial q'}{\partial t} + A \frac{\partial q'}{\partial x} + B_r \frac{\partial q'}{\partial r} + B_\theta \frac{\partial q'}{\partial \theta} + B_{xx} \frac{\partial^2 q'}{\partial x^2} + B_{rr} \frac{\partial^2 q'}{\partial r^2} + B_{\theta\theta} \frac{\partial^2 q'}{\partial \theta^2} + Lq' = 0. \quad (3)$$

The matrix coefficients are functions of the baseflow $\bar{q}(x, r)$ and are given in Appendix A.

We further simplify equation (3) by neglecting terms involving second axial derivatives. Although this is not necessary, it simplifies the process of decoupling the upstream and downstream dynamics contained within the linearized operator. These axial viscous terms have historically been neglected in previous spatial marching methods as well, such as the parabolized and reduced Navier-Stokes equations.¹⁸ Within the context of this work, omitting them is appropriate whenever the axial variation of the solution is much slower than the variation in the radial direction or when viscous effects are altogether unimportant in the linear evolution of the large-scale dynamics. The high-Reynolds-number jets considered in this paper in fact satisfy both of these conditions, suggesting that viscous terms could be neglected altogether. However, we have found that retaining the radial and azimuthal viscous terms helps stabilize spurious dynamics that in some cases impede the parabolization process. In that sense, the retained viscous terms can be thought of as regularization terms rather than physically important ones. Accordingly, we continue to refer to the equations as Euler equations despite the inclusion of the aforementioned viscous terms.

Next, the solution is discretized in the radial direction using N_r grid points and decomposed into Fourier modes in the azimuthal direction. We will use bold font to represent the discretized analogue of each variable and operator, and the azimuthal transform is indicated using superscript (\dagger) with the mode number specified by the subscript m . Equation (3) then becomes

$$\frac{\partial \mathbf{q}_m^\dagger}{\partial t} + \mathbf{A}(x) \frac{\partial \mathbf{q}_m^\dagger}{\partial x} + \mathbf{B}_m(x) \mathbf{q}_m^\dagger = \mathbf{0}, \quad (4)$$

where $\mathbf{B}_m = \mathbf{B}_r \mathbf{D}_r + im \mathbf{B}_\theta + \mathbf{B}_{rr} \mathbf{D}_{rr} + (im)^2 \mathbf{B}_{\theta\theta} + \mathbf{L}$. The matrices \mathbf{D}_r and \mathbf{D}_{rr} approximate the first and second radial derivatives, respectively. At this point, pole conditions and far-field radial boundary conditions are also incorporated into \mathbf{B}_m . Since each azimuthal mode is treated independently and identically, we drop the subscript m .

Equation (4) is a one-dimensional strongly hyperbolic system. In other words, \mathbf{A} is diagonalizable and has real eigenvalues. This follows directly from the fact that the undiscretized operator A satisfies these requirements, as shown in Appendix A. The eigenvalues of A are

$$\lambda_{1,2,3} = \bar{u}, \quad (5a)$$

$$\lambda_{3,4} = \bar{u} \pm \bar{c}, \quad (5b)$$

where \bar{u} and \bar{c} are the local axial velocity and sound speed. Evaluating these eigenvalues at each radial grid point gives the eigenvalues of \mathbf{A} . The number of positive, zero, and negative eigenvalues of \mathbf{A} will be important in the development of our parabolized equations. We denote these quantities as N_+ , N_0 , and N_- , respectively. Also define $N = N_+ + N_0 + N_- = 5N_r$. For a subsonic jet, the first four eigenvalues of A will be positive and λ_5 will be negative everywhere, so $N_+ = 4N_r$, $N_0 = 0$, and $N_- = N_r$. For a supersonic jet, λ_5 becomes positive in regions of supersonic flow, so we have $4N_r < N_+ < 5N_r$, $N_- < N_r$, and either $N_0 = 0$ or $N_0 = 1$, depending on whether a grid point coincides with the sonic point at a given axial location.

For the remainder of this paper, we will assume that N_+ and N_- are fixed for all x and that $N_0 = 0$. This is true for all subsonic flows, as well as supersonic parallel flows as long as a grid point does not coincide with the sonic point. It is not true for nonparallel supersonic jets, since the number of grid points within the sonic region changes as the jet spreads. This assumption is not necessary for the development of our parabolization method, but making it greatly simplifies the presentation.

It proves useful to work with the characteristic variables of equation (4). Since \mathbf{A} is diagonalizable, there exists a transformation $\mathbf{T}(x)$ such that

$$\mathbf{T} \mathbf{A} \mathbf{T}^{-1} = \tilde{\mathbf{A}} = \begin{bmatrix} \tilde{\mathbf{A}}_{++} & \mathbf{0} \\ \mathbf{0} & \tilde{\mathbf{A}}_{--} \end{bmatrix} \quad (6)$$

where $\tilde{\mathbf{A}}$, $\tilde{\mathbf{A}}_{++} \in \mathbb{R}^{N_+ \times N_+} > 0$, and $\tilde{\mathbf{A}}_{--} \in \mathbb{R}^{N_- \times N_-} < 0$ are diagonal matrices. The diagonal entries of $\tilde{\mathbf{A}}_{++}$ and $\tilde{\mathbf{A}}_{--}$ are precisely the positive and negative eigenvalues of \mathbf{A} , respectively. The transformation \mathbf{T} is known analytically since it is the discretization of the matrix T that diagonalizes A (see Appendix A).

The characteristic variables of equation (4) are then $\phi^\dagger(x, t) = \mathbf{T}(x) \mathbf{q}^\dagger(x, t)$, and can be separated into positive and negative parts based on the positive and negative blocks of \mathbf{A} :

$$\phi^\dagger = \begin{Bmatrix} \phi_+^\dagger \\ \phi_-^\dagger \end{Bmatrix} \quad (7)$$

with $\phi_+^\dagger \in \mathbb{R}^{N_+}$ and $\phi_-^\dagger \in \mathbb{R}^{N_-}$. In terms of the characteristic variables, equation (4) becomes

$$\frac{\partial \phi^\dagger}{\partial t} + \tilde{\mathbf{A}}(x) \frac{\partial \phi^\dagger}{\partial x} + \tilde{\mathbf{B}}(x) \phi^\dagger = \mathbf{0} \quad (8)$$

where $\tilde{\mathbf{B}} = \mathbf{T} \mathbf{B} \mathbf{T}^{-1} + \tilde{\mathbf{A}} \mathbf{T} \frac{d\mathbf{T}^{-1}}{dx}$.

Since we wish to obtain modal solutions, we proceed by applying a Laplace transform in time to equation (8), giving

$$s \hat{\phi} + \tilde{\mathbf{A}}(x) \frac{\partial \hat{\phi}}{\partial x} + \tilde{\mathbf{B}}(x) \hat{\phi} = \mathbf{0}, \quad (9)$$

where $\hat{\phi}(x, s)$ is the Laplace transform of $\phi^\dagger(x, t)$ and $s = \eta - i\omega$ ($\eta, \omega \in \mathbb{R}$) is the Laplace dual of t .

We have assumed zero initial conditions, but that is not important since we are not interested in transient start-up effects, but rather the long-time stationary behavior of the flow. We will ultimately take $\eta = 0$ and set ω to a particular value to obtain the modal solution at that frequency, but keeping the possibility of non-zero η will help us distinguish between upstream and downstream solutions of equation (8).

Solving equation (9) for x -derivatives then gives

$$\frac{d\hat{\phi}}{dx} = \mathbf{M}(x, s)\hat{\phi} \quad (10)$$

with

$$\mathbf{M} = -\tilde{\mathbf{A}}^{-1} (s\mathbf{I} + \tilde{\mathbf{B}}). \quad (11)$$

It is useful to divide \mathbf{M} into blocks according to the sizes of the positive and negative characteristic variables:

$$\frac{d}{dx} \begin{Bmatrix} \hat{\phi}_+ \\ \hat{\phi}_- \end{Bmatrix} = \begin{bmatrix} \mathbf{M}_{++} & \mathbf{M}_{+-} \\ \mathbf{M}_{-+} & \mathbf{M}_{--} \end{bmatrix} \begin{Bmatrix} \hat{\phi}_+ \\ \hat{\phi}_- \end{Bmatrix}. \quad (12)$$

The size of each block is implied by the subscripts; for example, $\mathbf{M}_{+-} \in \mathbb{C}^{N_+ \times N_-}$. We will continue to use this convention throughout the paper.

II.B. Exact Parabolization

In this subsection, we derive an exact parabolization of equation (10) for the special case of parallel flow (\mathbf{M} not a function of x). The method will be generalized to allow for non-parallel flow in section II.D. We also restrict our attention, for the remainder of the paper, to the case where \mathbf{M} is diagonalizable. The modifications required to accommodate a defective \mathbf{M} are straightforward but cumbersome, so we omit them for the sake of clarity.

The essential step in parabolizing equation (10) is distinguishing between its upstream propagating and downstream propagating solutions. Since equation (10) is uniform in x , its general solution is the summation of modes

$$\hat{\phi}(x, s) = \sum_{k=1}^N \mathbf{v}_k(s) \psi_k(x, s), \quad (13)$$

where each expansion coefficient ψ_k satisfies

$$\frac{d\psi_k}{dx} = i\alpha_k(s)\psi_k, \quad (14)$$

and each $(i\alpha_k, \mathbf{v}_k)$ is an eigenvalue-eigenvector pair of \mathbf{M} . We include the i in our definition of the eigenvalue for consistency with the usual definition of spatial wave-numbers. The real and imaginary parts of α_k are related to the phase-speed and growth rate of the mode.

The task at hand is to determine which of these modes are upstream propagating and which are downstream propagating, in terms of energy transfer. Briggs¹⁹ developed a criterion for making this distinction: mode k is downstream propagating if $\lim_{\eta \rightarrow +\infty} \Im[\alpha_k(s)] = +\infty$ and upstream propagating if $\lim_{\eta \rightarrow +\infty} \Im[\alpha_k(s)] = -\infty$. Since \mathbf{M} tends to the real diagonal matrix $-\eta\tilde{\mathbf{A}}^{-1}$ as $\eta \rightarrow +\infty$, it is clear that all of its eigenvalues will exhibit one of these two behaviors. Furthermore, based on the block structure of $\tilde{\mathbf{A}}$, there are exactly N_+ downstream modes and N_- upstream modes. When applied to an operator obtained from a constant coefficient hyperbolic system such as equation (10), Briggs' criterion is consistent with well-posedness theory for hyperbolic systems as developed by Kreiss.²⁰

The exact parabolization of equation (10) is then obtained by zeroing the upstream modes. That is, for each upstream mode, equation (14) is replaced with the condition

$$\psi_k = 0. \quad (15)$$

This is exactly the same condition that is applied to each upstream mode in order to generate non-reflecting boundary conditions at an outflow. Indeed, our parabolization technique can be thought of as applying a non-reflecting outflow boundary condition everywhere.

In order to write the parabolized system clearly and compactly, it is useful to write it in block matrix form. First, the expansion coefficients are arranged in a vector $\boldsymbol{\psi}$ such that the the N_+ downstream modes appear first followed by the N_- upstream modes:

$$\boldsymbol{\psi} = \begin{Bmatrix} \boldsymbol{\psi}_+ \\ \boldsymbol{\psi}_- \end{Bmatrix}. \quad (16)$$

Then equation (13) and equation (14) can be written in matrix form as

$$\hat{\boldsymbol{\phi}} = \mathbf{V}\boldsymbol{\psi} \quad \leftrightarrow \quad \boldsymbol{\psi} = \mathbf{U}\hat{\boldsymbol{\phi}} \quad (17)$$

and

$$\frac{d\boldsymbol{\psi}}{dx} = \mathbf{D}\boldsymbol{\psi}. \quad (18)$$

The columns of \mathbf{V} are the right eigenvectors, the rows of $\mathbf{U} = \mathbf{V}^{-1}$ are the left eigenvectors, and the entries of the diagonal matrix \mathbf{D} are the eigenvalues of \mathbf{M} , all ordered in the same way as $\boldsymbol{\psi}$, such that $\mathbf{M} = \mathbf{V}\mathbf{D}\mathbf{U}$.

We can also partition the matrices \mathbf{D} , \mathbf{V} , and \mathbf{U} into blocks based on their association with the upstream and downstream expansion coefficients and the positive and negative characteristic variables. Specifically, we write

$$\frac{d}{dx} \begin{Bmatrix} \boldsymbol{\psi}_+ \\ \boldsymbol{\psi}_- \end{Bmatrix} = \begin{bmatrix} \mathbf{D}_{++} & \mathbf{0} \\ \mathbf{0} & \mathbf{D}_{--} \end{bmatrix} \begin{Bmatrix} \boldsymbol{\psi}_+ \\ \boldsymbol{\psi}_- \end{Bmatrix}, \quad (19)$$

$$\begin{Bmatrix} \hat{\boldsymbol{\phi}}_+ \\ \hat{\boldsymbol{\phi}}_- \end{Bmatrix} = \begin{bmatrix} \mathbf{V}_{++} & \mathbf{V}_{+-} \\ \mathbf{V}_{-+} & \mathbf{V}_{--} \end{bmatrix} \begin{Bmatrix} \boldsymbol{\psi}_+ \\ \boldsymbol{\psi}_- \end{Bmatrix}, \quad (20)$$

and

$$\begin{Bmatrix} \boldsymbol{\psi}_+ \\ \boldsymbol{\psi}_- \end{Bmatrix} = \begin{bmatrix} \mathbf{U}_{++} & \mathbf{U}_{+-} \\ \mathbf{U}_{-+} & \mathbf{U}_{--} \end{bmatrix} \begin{Bmatrix} \hat{\boldsymbol{\phi}}_+ \\ \hat{\boldsymbol{\phi}}_- \end{Bmatrix}. \quad (21)$$

Recall that based on our ordering of $\boldsymbol{\psi}$, \mathbf{D}_{++} contains the downstream eigenvalues and \mathbf{D}_{--} contains the upstream eigenvalues.

The exact parabolization of equation (10), in terms of $\boldsymbol{\psi}$, is then

$$\frac{d\boldsymbol{\psi}_+}{dx} = \mathbf{D}_{++}\boldsymbol{\psi}_+, \quad (22a)$$

$$\boldsymbol{\psi}_- = \mathbf{0}. \quad (22b)$$

This can also be written in terms of the characteristic variables as

$$\frac{d\hat{\boldsymbol{\phi}}_+}{dx} = \mathbf{M}_{++}\hat{\boldsymbol{\phi}}_+ + \mathbf{M}_{+-}\hat{\boldsymbol{\phi}}_-, \quad (23a)$$

$$\mathbf{U}_{-+}\hat{\boldsymbol{\phi}}_+ + \mathbf{U}_{--}\hat{\boldsymbol{\phi}}_- = \mathbf{0}. \quad (23b)$$

When \mathbf{U}_{--} is invertible, equation (23) is a differential-algebraic system of index 1 and $\hat{\boldsymbol{\phi}}_-$ can be eliminated, giving an ordinary differential equation for the positive characteristic variable:

$$\frac{d\hat{\boldsymbol{\phi}}_+}{dx} = \mathbf{P}\hat{\boldsymbol{\phi}}_+, \quad (24)$$

where

$$\mathbf{P} = \mathbf{M}_{++} - \mathbf{M}_{+-}\mathbf{U}_{--}^{-1}\mathbf{U}_{-+} \quad (25a)$$

$$= \begin{bmatrix} \mathbf{M}_{++} & \mathbf{M}_{+-} \end{bmatrix} \begin{bmatrix} \mathbf{I} \\ -\mathbf{U}_{--}^{-1}\mathbf{U}_{-+} \end{bmatrix} \quad (25b)$$

$$= \begin{bmatrix} \mathbf{V}_{++} & \mathbf{V}_{+-} \end{bmatrix} \begin{bmatrix} \mathbf{D}_{++} & \mathbf{0} \\ \mathbf{0} & \mathbf{D}_{--} \end{bmatrix} \begin{bmatrix} \mathbf{U}_{++} & \mathbf{U}_{+-} \\ \mathbf{U}_{-+} & \mathbf{U}_{--} \end{bmatrix} \begin{bmatrix} \mathbf{I} \\ -\mathbf{U}_{--}^{-1}\mathbf{U}_{-+} \end{bmatrix} \quad (25c)$$

$$= \begin{bmatrix} \mathbf{V}_{++} & \mathbf{V}_{+-} \end{bmatrix} \begin{bmatrix} \mathbf{D}_{++} & \mathbf{0} \\ \mathbf{0} & \mathbf{D}_{--} \end{bmatrix} \begin{bmatrix} \mathbf{V}_{++}^{-1} \\ \mathbf{0} \end{bmatrix} \quad (25d)$$

$$= \mathbf{V}_{++}\mathbf{D}_{++}\mathbf{V}_{++}^{-1}. \quad (25e)$$

In going from the third to fourth line, we made use of the identity $\mathbf{V}_{++}^{-1} = \mathbf{U}_{++} - \mathbf{U}_{+-}\mathbf{U}_{--}^{-1}\mathbf{U}_{-+}$. It is clear from the final equality that the eigenvalues of \mathbf{P} are precisely the downstream eigenvalues of \mathbf{M} .

Implementation of the exact one-way equation given by equation (23) would require calculation of the N_- left eigenvectors corresponding to the upstream eigenvalues of \mathbf{M} . The resulting computational cost is usually intolerably high. This is especially true for nonparallel flows, in which case local eigenvectors would need to be calculated at each x (see section II.D). Instead, we will generate a practical one-way equation by approximating the parabolization condition given by equation (23b).

II.C. Approximate Parabolization

Motivated by the connection between the exact parabolization method and non-reflecting boundary conditions, our approximate parabolization method is based on recursions that were introduced by Givoli & Neta²¹ and Hagstrom & Warburton²² for generating non-reflecting boundary conditions. Accordingly, we propose an approximate parabolization given by the differential-algebraic system

$$\frac{d\hat{\phi}_+}{dx} = \mathbf{M}_{++}\hat{\phi}_+ + \mathbf{M}_{+-}\hat{\phi}_-, \quad (26a)$$

$$\left(\mathbf{M} - \imath b_+^j \mathbf{I}\right) \hat{\phi}^j = \left(\mathbf{M} - \imath b_-^j \mathbf{I}\right) \hat{\phi}^{j+1} \quad j = 0, \dots, N_b - 1, \quad (26b)$$

$$\hat{\phi}_-^{N_b} = 0. \quad (26c)$$

In this formulation, we have introduced a set of auxiliary variables $\{\hat{\phi}^j : j = 0, \dots, N_b\}$ and a set of complex scalar parameters $\{b_+^j, b_-^j : j = 0, \dots, N_b - 1\}$. The zero-indexed variable is the physical variable ($\hat{\phi}^0 = \hat{\phi}$) and the remaining auxiliary variables are defined by the recursions. The selection of the parameters will be discussed below. We call N_b the order of the approximate one-way equation.

We will now show that the approximate one-way equation given by equation (26) converges to the exact one-way equation equation (23) in the limit $N_b \rightarrow \infty$ when the recursion parameters are appropriately chosen. Since equation (26a) is identical to equation (23a), we must only show that equation (26b) and equation (26c) together converge to equation (23b). In other words, we wish to show that $\psi_- \rightarrow \mathbf{0}$ as $N_b \rightarrow \infty$. To do so, we begin by defining $\psi^j = \mathbf{U}\hat{\phi}^j$, which is the natural extension of the previous definition $\psi = \mathbf{U}\hat{\phi}$. Equation (26b) can then be written

$$\left(\mathbf{D} - \imath b_+^j \mathbf{I}\right) \psi^j = \left(\mathbf{D} - \imath b_-^j \mathbf{I}\right) \psi^{j+1} \quad j = 0, \dots, N_b - 1. \quad (27)$$

Since \mathbf{D} is diagonal, each scalar component of ψ^j can be considered separately:

$$\left(\imath\alpha_k - \imath b_+^j\right) \psi_k^j = \left(\imath\alpha_k - \imath b_-^j\right) \psi_k^{j+1} \quad j = 0, \dots, N_b - 1, k = 1, \dots, N. \quad (28)$$

It is then straightforward to eliminate all of the intermediate ($j = 1, \dots, N_b - 1$) auxiliary variables, leaving

$$\psi_k^{N_b} = \left(\prod_{j=0}^{N_b-1} \frac{\alpha_k - b_+^j}{\alpha_k - b_-^j} \right) \psi_k \quad k = 1, \dots, N. \quad (29)$$

For every k , the coefficient relating $\psi_k^{N_b}$ and ψ_k is the value of a function that is independent of k , evaluated at α_k . That is,

$$\psi_k^{N_b} = \mathcal{F}(\alpha_k) \psi_k \quad k = 1, \dots, N. \quad (30)$$

with

$$\mathcal{F}(\alpha) = \prod_{j=0}^{N_b-1} \frac{\alpha - b_+^j}{\alpha - b_-^j}. \quad (31)$$

We now re-assemble equation (30) into a single matrix equation for all k :

$$\begin{Bmatrix} \psi_+^{N_b} \\ \psi_-^{N_b} \end{Bmatrix} = \begin{bmatrix} \mathbf{F}_{++} & \mathbf{0} \\ \mathbf{0} & \mathbf{F}_{--} \end{bmatrix} \begin{Bmatrix} \psi_+ \\ \psi_- \end{Bmatrix}. \quad (32)$$

where \mathbf{F}_{++} and \mathbf{F}_{--} are diagonal matrices whose entries are \mathcal{F} evaluated at each rightgoing and leftgoing eigenvalue, respectively. In other words, $\mathbf{F}_{++} = \mathcal{F}(\mathbf{D}_{++})$ and $\mathbf{F}_{--} = \mathcal{F}(\mathbf{D}_{--})$.

Next, we apply the termination condition given by equation (26c). To do so, we write the left-hand-side of equation (32) in terms of $\hat{\phi}^{N_b}$:

$$\begin{bmatrix} \mathbf{U}_{++} & \mathbf{U}_{+-} \\ \mathbf{U}_{-+} & \mathbf{U}_{--} \end{bmatrix} \begin{Bmatrix} \hat{\phi}_+^{N_b} \\ \hat{\phi}_-^{N_b} \end{Bmatrix} = \begin{bmatrix} \mathbf{F}_{++} & \mathbf{0} \\ \mathbf{0} & \mathbf{F}_{--} \end{bmatrix} \begin{Bmatrix} \psi_+ \\ \psi_- \end{Bmatrix}. \quad (33)$$

Applying equation (26c) leaves

$$\begin{bmatrix} \mathbf{U}_{++} \\ \mathbf{U}_{-+} \end{bmatrix} \hat{\phi}_+^{N_b} = \begin{bmatrix} \mathbf{F}_{++} & \mathbf{0} \\ \mathbf{0} & \mathbf{F}_{--} \end{bmatrix} \begin{Bmatrix} \psi_+ \\ \psi_- \end{Bmatrix}. \quad (34)$$

When \mathbf{U}_{++} is invertible, $\hat{\phi}_+^{N_b}$ can be eliminated, giving

$$\psi_- = \mathbf{R}\psi_+ \quad (35)$$

with

$$\mathbf{R} = -\mathbf{F}_{--}^{-1}\mathbf{U}_{-+}\mathbf{U}_{++}^{-1}\mathbf{F}_{++}. \quad (36)$$

The rectangular matrix \mathbf{R} is analogous to a matrix of reflection coefficients. To attain $\psi_- \rightarrow \mathbf{0}$, the recursion parameters must be chosen such that each entry in \mathbf{R} approaches zero. In practice, this requires some knowledge regarding the approximate locations of the upstream and downstream eigenvalues. Typically, the Euler equation supports convective modes that travel with phase velocities ranging from the slowest to fastest axial velocities in the flow. Additionally, the Euler equations usually support acoustic modes that are well approximated by treating them as acoustic modes in a uniform free stream. Such modes are solutions of the convective Helmholtz equation with uniform velocity \bar{u}_x . The eigenvalues are

$$\alpha_{\pm}(z) = k \frac{-\bar{u}_x \pm \mu(z)}{1 - \bar{u}_x^2} \quad (37)$$

with

$$\mu(z) = \sqrt{1 - (1 - \bar{u}_x^2)z^2} \quad (38)$$

and $z \in (0, \infty)$.

The simplest strategy for selecting the recursion parameters is to choose a single pair $\{b_+^j, b_-^j\}$ for which $\mathcal{F} < 1$ for all downstream eigenvalues and $\mathcal{F} > 1$ for all upstream eigenvalues, and use this pair for all $j = 0, \dots, N_b - 1$. If we define κ to be the product of the maximum entries of \mathbf{F}_{++} and \mathbf{F}_{--}^{-1} for $N_b = 1$, then the magnitude of the slowest converging entry of \mathbf{R} will decrease like $|\kappa|^{N_b}$. Therefore, even for this very simple choice of parameters, the method exhibits spectral convergence.

It is not always possible to find a single pair of recursion parameters that meets the above requirements. Even when it is possible, it is typically preferable to distribute the parameters over a range of locations based on the expected values of the upstream and downstream eigenvalues in an attempt to minimize \mathbf{R} at a given N_b rather than to guarantee a certain rate of convergence.

Most of the results in this paper are obtained using the following strategy. Some of the parameters, usually about half, are distributed along the real axis over the range of convective phase speeds supported by the baseflow. The remaining parameters are placed along the acoustic branches given in equation (37) by varying z from 0 to the maximum value supported by the mesh with \bar{u}_x set to some characteristic velocity of the flow.

This approach to parameter selection is certainly not optimal. Within the context of nonreflecting boundary conditions for uniform flow Euler equations, parameters have been derived that are optimal at every N_b and guarantee spectral convergence.²³ However, these parameters are fundamentally linked to the time-domain and cannot be easily translated to the frequency domain. Finding robust, optimal frequency domain parameters is an ongoing aspect of our work.

II.D. Extension to non-parallel flows

In the previous two subsections, we developed exact and approximate parabolization techniques for the Euler equations under the assumption of parallel flow. In this subsection, we discuss the extension of these methods to non-parallel flow.

First, it is easy to verify that for a nonparallel flow, the approximate parabolization given by equation (26) still converges to the exact parabolization given by equation (23) at every x . Therefore, we must only evaluate the exact method, and all conclusions will apply also to the approximate formulation.

Central to the concept of parabolization is the identification of upstream and downstream parts of the solution at each axial location. When \mathbf{M} depends on x , equation (10) no longer admits simple modal solutions, so Briggs' criterion no longer strictly applies. However, the theory of well-posedness of variable coefficient hyperbolic systems²⁰ provides a means by which to distinguish, locally at each x , parts of the solution that are propagated upstream and downstream. Simply put, the variable coefficient extension of well-posedness theory states that constant coefficient analysis of the frozen coefficient system at a given x provides the correct (that is, well-posed) division of the solution into upstream and downstream components. Therefore, the one-way equations derived in the previous two sections will still retain and eliminate the correct parts of the Euler operator at each axial station in non-parallel flows.

The fundamental difference between the parallel and non-parallel cases is that in a non-parallel flow, the upstream and downstream variables no longer evolve independently. Except in rare cases, the transformation $\boldsymbol{\psi} = \mathbf{U}\hat{\boldsymbol{\phi}}$ no longer diagonalizes equation (10) because $\frac{d\mathbf{U}}{dx} \neq \mathbf{0}$. As a result, every expansion coefficient ψ_k is potentially coupled with every other coefficient, so the upstream and downstream variables no longer evolve independently. This coupling is intrinsic to non-parallel flow equations and is deeply linked to important properties of their solutions. For example, this coupling allows convective waves in jets to excite acoustic waves that propagate in all directions.

The implication of this coupling for our one-way equation is that setting $\boldsymbol{\psi}_- = \mathbf{0}$ will cause $\boldsymbol{\psi}_+$ to evolve incorrectly as it propagates downstream. If for a given problem the upstream waves significantly interact with and modify the downstream waves, this error will become large and an accurate one-way spatial marching solution is not possible. If, however, the coupling between the upstream and downstream parts of the solution is sufficiently weak, an accurate one-way solution can be obtained.

An important situation in which the coupling is weak occurs when the baseflow is *slowly-varying* in x . In this case, the slow variation of the baseflow ensures the slow variation of \mathbf{U} , which in turn implies that \mathbf{U} nearly diagonalizes \mathbf{M} . A close examination of the meaning of "nearly diagonalizes" reveals that this is akin to the usual short-wavelength condition that is frequently invoked when applying parallel theory to non-parallel flows. To reiterate, the one-way Euler equations are well-posed for all parallel and non-parallel flows, but accuracy is guaranteed only for sufficiently slowly varying baseflows.

II.E. Computational Cost

Using the approximate one-way Euler method entails satisfying the differential-algebraic system given by equation (26) at each axial step in the march. This, in turn, requires the solution of a matrix system with leading dimension $\mathcal{O}(N_r N_b)$. For efficiency, it is important for the system to be sparse, which requires the use of a sparse discretization schemes. When this requirement is observed, the banded structure of the system results in a predicted operation count that scale like $N_r N_b^2$. Modern sparse solvers can often exploit additional structure within the system not accounted for in this cost estimate, so in practice we observe scaling like $N_r N_b^p$ with $1 < p < 2$. Frequently, $p \approx 1.5$.

The eigen-solution required by the exact parabolization method scales like N_r^3 . The cost savings of the approximate method stems from the fact that $N_b \ll N_r$ and therefore $N_b^p \ll N_r^2$. Because of the impracticality of the exact parabolization method, from here on out we will refer to the approximate method as *the* one way Euler method.

In comparison, PSE usually scales like $N_r N_{it}$, where N_{it} is the number of iterations required to satisfy a nonlinear constraint that is part of the PSE formulation. Finally, direct time domain and frequency domain solutions of the full Euler equations scale like $N_r N_t$ and N_r^2 , respectively, per axial station. In time domain solvers, N_t is the number of time step required to obtain a stationary solution. Again, the benefit of the one-way Euler method is that $N_b^p \ll N_t$.

III. Validation

This section contains two test problems used to verify the convergence and accuracy of our one-way Euler formulation. First, we demonstrate convergence to an exact solution for the simple case of acoustic waves generated by a monopole in a free-stream. Second, the accuracy of previously reported results for a two-dimensional mixing layer are confirmed by comparing the one-way Euler solution to a direct solution of the linearized Euler equations. Results for both test problems are also compared to PSE solutions to highlight the improvement achieved by the one-way Euler method.

For all simulations in this section and section IV, the equations are discretized in the radial (or transverse) direction using fourth-order central finite differences with summation-by-parts boundary closure.²⁴ Radiation boundary conditions are enforced using a super-grid damping layer^{25,26} truncated by Thompson characteristic conditions.²⁷ Pole conditions are implemented using the scheme of Mohseni & Colonius.²⁸ For the one-way Euler equations, we perform the downstream march using a fourth-order diagonally-implicit Runge-Kutta scheme, while PSE uses implicit Euler integration by definition.

III.A. Monopole forcing

In this problem, a monopole disturbance is placed just upstream of the computational domain in a Mach 0.25 uniform, inviscid free stream. The monopole generates an axisymmetric acoustic field, shown in figure 1(a), for which an analytical solution exists. Along the inlet of the computational domain, indicated by the vertical dashed line, the exact solution is supplied as an initial condition to the one-way Euler and PSE algorithms. Then, this solution is propagated downstream by the spatial marching routine of each method, and the error in each solution is calculated by comparison to the analytical solution. Since the flow is parallel and the solution is comprised exclusively of downstream propagating waves, this set-up allows the convergence of the one-way equation to be verified.

The recursion parameters for the one-way Euler method are chosen as follows. The first parameter b_+^1 is chosen to coincide with the discrete convective mode $\alpha = \omega/\bar{u}_x$, and the corresponding b_-^1 is the reflection of b_+^1 over the line $\Im[\alpha] = -\Re[\alpha]$. The second parameter pair is chosen to be $(b_+^2, b_-^2) \approx (3 + 6i, -9 - 6i)$. All additional parameter pairs repeat this second pair.

Figure 1(b) contains the error results. The error in this plot is defined as the local difference between the numerical and analytical solution normalized by the local analytical solution and integrated over the $x - r$ plane at a fixed θ . The convergence of the one-way Euler solution over $1 < N_b < 5$ is roughly spectral, as expected. For $N_b > 5$, the error plateaus at a level equal to the error of the exact parabolization method. Recall that the one-way Euler eigenvalues converge toward the eigenvalues of the *discretized* equations. The properties of the underlying discretization – both good and bad – are unaltered by the parabolization method. Therefore, the convergence plateau indicates that the discretization error has become larger than the parabolization error. By the time this occurs, the one-way Euler error is over three orders of magnitude smaller than the PSE error. Note that the PSE calculations reported here are best case results in the sense that the most energetic acoustic mode was initialized as the primary PSE mode.

A useful way to visualize the convergence of the parabolization procedure is to compare the eigenvalues of the one-way Euler operator to those of the full Euler operator \mathbf{M} . Figure 2(a) shows the spectrum of the full Euler operator for this problem. Note that additional stable convective modes exist, but are omitted from the plot so that the behavior of the more important acoustic modes can be clearly presented. The remaining subfigures show the spectra for several orders of the one-way Euler operator as well as the exact one-way operator. At $N_b = 0$, the upstream acoustic waves have been removed, but the downstream eigenvalues are poorly represented. The very small angle downstream propagating waves are properly captured while all other waves are poorly modeled. As N_b is increased, all downstream eigenvalues continue to converge toward the spectrum of the full Euler operator, so that more and more of the downstream acoustic modes are properly modeled.

III.B. Two-dimensional mixing layer

Here, we confirm the accuracy of a previous result¹⁷ in which the generation and propagation of sound in a two-dimensional mixing layer was modeled using one-way Euler equations. This problem demonstrates the accuracy of the method for slowly-varying nonparallel flows.

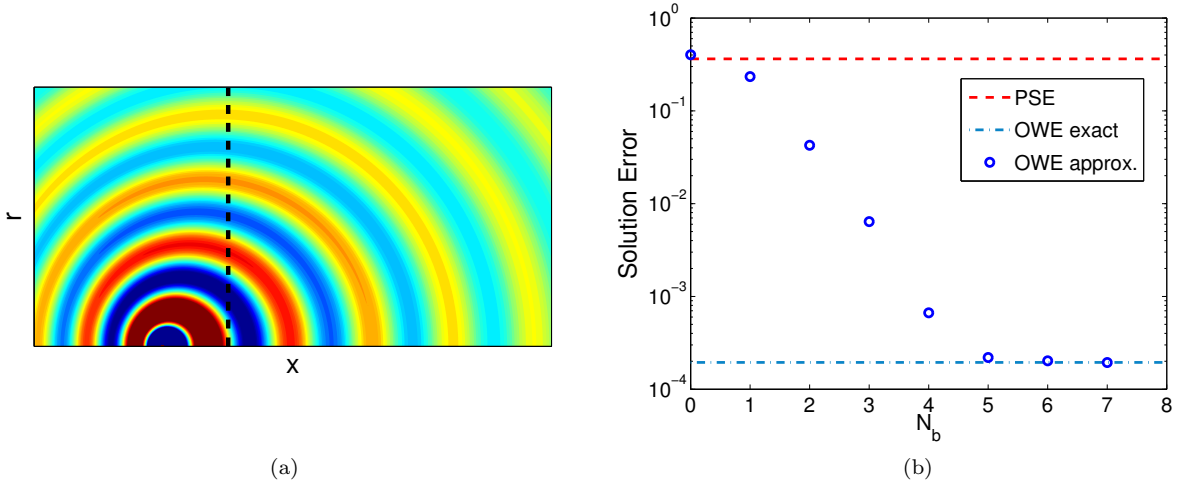


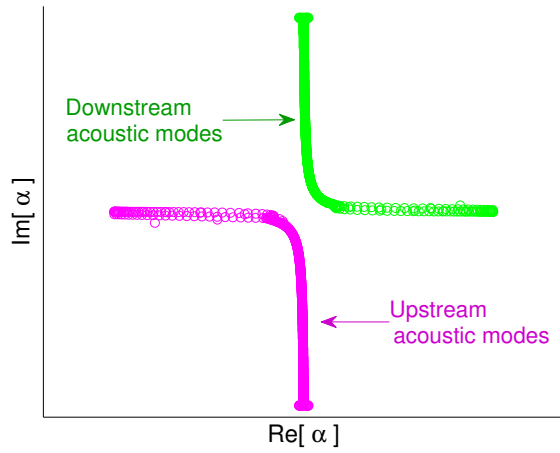
Figure 1: Monopole test case. (a) real part of the exact pressure field created by the monopole. The dashed line shows the location where the initial condition is specified for the marching procedures. (b) global error of the one-way Euler equations, PSE, and exact one-way Euler equations compared to the exact solution. Error is defined as $\|(\hat{p} - \hat{p}_{exact})/\hat{p}_{exact}\|$ integrated over the full computational domain.

The baseflow is a second-order approximation of a self-similar solution of the incompressible boundary layer equations using Prandtl’s eddy viscosity model.²⁹ The Mach number of the fast and slow free-streams are 0.8 and 0.2, respectively. The shear layer thickness grows linearly, with the spread rate chosen to match experiments. The initial condition at the inlet is a pure Kelvin-Helmholtz eigenfunction computed at $x = 0$ under a locally-parallel assumption. We show results for the most unstable frequency near the inlet. The solution is computed using the PSE and the approximate one-way Euler equations at $N_b = 15$. The one-way Euler solution is well-converged at this order. The exact one-way Euler solution is prohibitively expensive for this problem and is not computed. See the original paper (Towne & Colonius, 2013) for additional details.

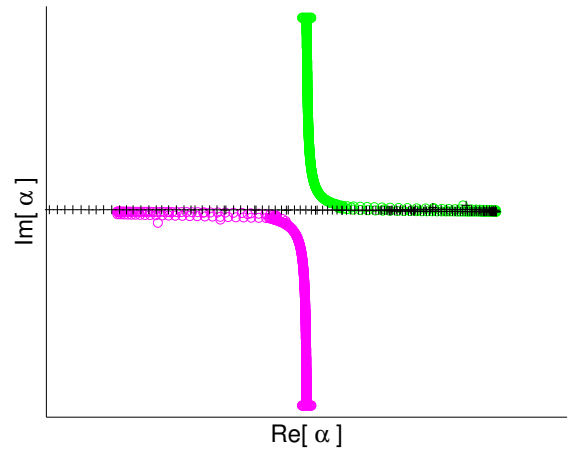
The accuracy of the one-way Euler solution is verified by comparing it to a direct solution of the linearized Euler equations (LEE). Precisely, equation (10) is solved as a boundary-value-problem by applying non-reflecting boundary conditions at the limits of the axial domain and discretizing in x . The result is a very large, sparse matrix equation in which the right-hand-side vector is created by specifying the same inlet condition used for the marching methods, and the unknown vector is the solution at all x and y grid points. Since equation (10) is properly treated as a boundary-value-problem, the LEE solution fully accounts for the non-parallel baseflow, and therefore can be considered the correct solution for this problem, up to numerical error.

Figure 3 shows the pressure field as computed by LEE, PSE, and OWE. First, consider the LEE solution. The near-field is dominated by a growing, then decaying wavepacket. The location where the wavepacket begins to decay acts as a sound source, creating acoustic radiation in all directions but especially in the downstream direction in the slow-stream ($y < 0$). Comparing the PSE and LEE solutions, two deficiencies are clearly discernible. First the PSE near-field wavepacket decays too rapidly. Second, the PSE solution contains almost no acoustic field at all. Again, this is due to the fact that the downstream acoustic modes in the PSE equations were heavily damped to allow a stable march.

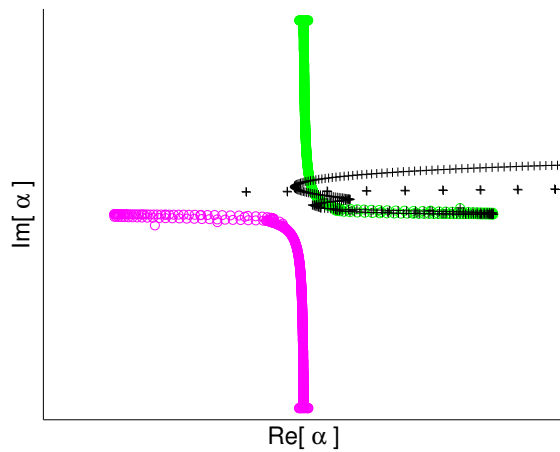
The one-way Euler solution does not suffer from either of these problems. The near-field wavepacket in the one-way Euler solution is indistinguishable from the LEE wavepacket, and the downstream acoustic radiation is accurately captured. Two differences can be identified between the LEE and one-way Euler solutions. First, the one-way Euler solution does not capture the upstream acoustic radiation. This is inherent to any spatial marching technique. Second, the downstream acoustic radiation to very high angles is somewhat inaccurate. This occurs because the eigenvalues associated with high angle acoustic radiation are typically difficult to converge. This error can be reduced by increasing the order of the recursions, but in many applications, including jet aeroacoustics, this high angle sound is unimportant compared to low angle sound, which is well captured using fairly lower order recursions.



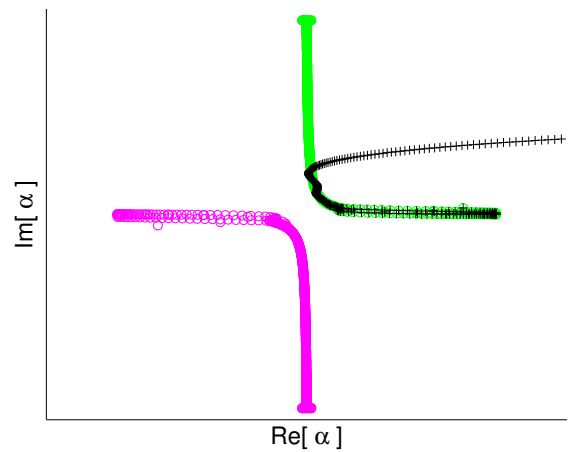
(a) Full Euler



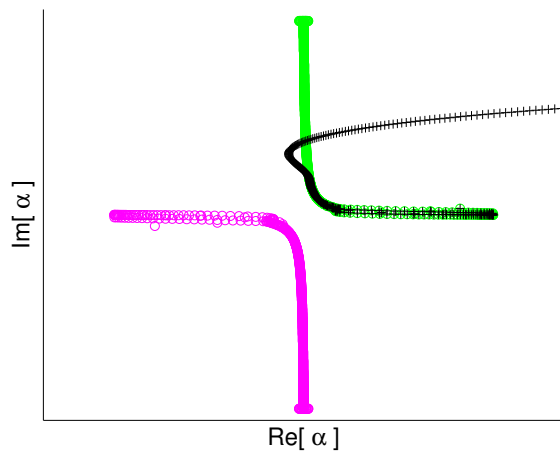
(b) $N_b = 0$



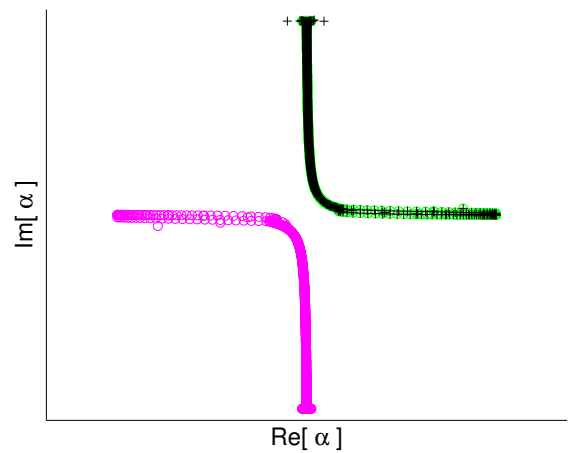
(c) $N_b = 2$



(d) $N_b = 4$



(e) $N_b = 6$



(f) Exact

Figure 2: Convergence of the spectrum of the one-way operator (+) to the downstream acoustic modes of the full Euler operator (green \circ). The upstream waves are completely removed and the downstream waves converge spectrally. The spectrum of the exact one-way operator is shown in (f).

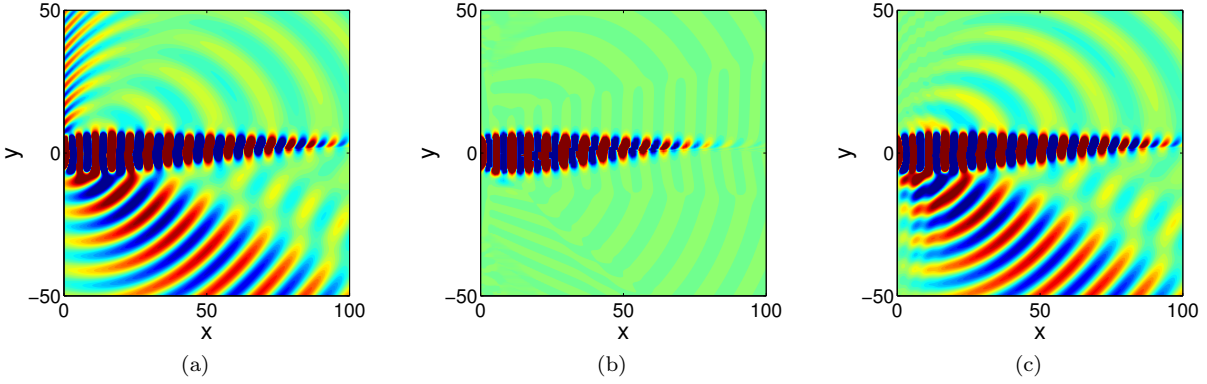


Figure 3: Pressure field generated by a wavepacket in a turbulent mixing layer computed using (a) direct solution of the linearized Euler equations, (b) PSE, (c) the one-way Euler equations.

Figure 4(a) shows the pressure field along $x = 50$ for each method. The exponential decay of the near-field pressure in all of the solutions is consistent with the asymptotic behavior of the Kelvin-Helmholtz mode. The LEE and one-way Euler pressure fields level off due to the presence of propagating acoustic waves that radiate to the far-field, and the agreement between these two solutions is excellent. In contrast, the damped remnants of acoustic radiation in the PSE solution is at least four orders of magnitude too small. Figure 4(b) shows the pressure field along a circular arc of radius 50 centered at the origin passing through the slow stream. It is clear that the primary error in the one-way Euler pressure field occurs at high angles, and that the solution at low and intermediate angles is in close agreement with the LEE solution.

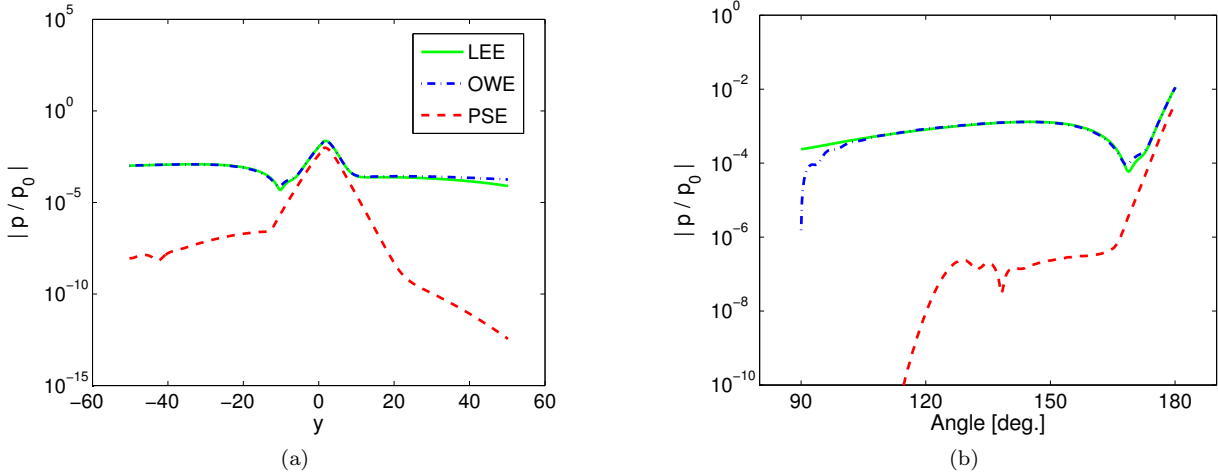


Figure 4: LEE, OWE, and PSE pressure amplitude for the turbulent mixing layer (a) along the transverse slice $x = 50$ (b) along a circular arc of radius 50 centered at the origin, sweeping through the slow stream. The angle is measured counter-clockwise from the negative x -axis.

Recall that the purpose of developing an improved spatial marching technique was to efficiently obtain accurate modal solutions. We have seen here that the one-way Euler equations can produce accurate results. Table 1 shows the improved efficiency obtained over the direct LEE method for this mixing layer problem. Compared to LEE, the one-way Euler method offers a speed-up of 42 times and a factor of 242 times reduction in memory usage. We note that time domain implementations of the linearized Euler equations are less memory intensive than the frequency domain solver used here, but they are also slower, so the one-way Euler method would also offer attractive savings over time domain LEE solvers. The low CPU and RAM requirements of PSE are achieved at the expense of accuracy, as we have seen.

Method	CPU Hours	RAM (GB)
LEE	136.0	194.1
OWE	3.2	0.8
PSE	0.02	0.08

Table 1: Computational costs for the mixing layer problem

IV. Results

In this section, we present results related to the application of the one-way Euler equations to jets. First, we demonstrate the ability of the parabolized equations to accurately represent the typical eigen-families that exist in supersonic and subsonic parallel jets, and in particular highlight the improved representation of important low-angle acoustic eigenvalues. Second, we calculate modal solutions of a Mach 0.5 turbulent jet over a range of Strouhal numbers using the one-way Euler equations and compare these results to those obtained using PSE.

IV.A. Parallel Jets

Here, we apply the one-way Euler method to supersonic and subsonic parallel jets. The base axial velocity is taken as

$$\bar{u}_x = \frac{\bar{u}_{jet} - \bar{u}_{co}}{2} \left(1 + \tanh \left(\frac{1}{4H} \left(\frac{1}{2r} - 2r \right) \right) \right) + \bar{u}_{co}, \quad (39)$$

where \bar{u}_{jet} is the jet velocity, \bar{u}_{co} is the co-flow velocity, and H controls the momentum thickness of the shear-layer. With properly chosen H , this profile fits well with experimentally measured velocity profiles near the end of the potential core.⁵ In the following sections, we study a Mach 1.5 jet with a Mach 0.1 co-flow and a Mach 0.9 jet with a Mach 0.1 co-flow. For both cases, we use the experimentally motivated thickness parameter $H = 0.16$.³⁰ The pressure and specific volume are taken to be constant, and the radial and azimuthal velocities are zero.

The computational domain extends five jet diameters in the radial direction, and the radial coordinate is discretized using 350 points. A coordinate transformation is used to cluster grid-points in the shear-layer. Additional computational details are given at the beginning of Section III. Even though our discretization is stable in the inviscid limit, we use a Reynolds number of one million to further damp all spurious modes.

IV.A.1. Full Euler Spectrum

The spatial spectra of the Euler and Navier-Stokes equations for parallel supersonic and subsonic jets have been extensively studied by a large number of investigators.^{6, 30-32} Within different flow regimes, several distinct families of modes have been identified and characterized. Although jet spectra have been shown to be sensitive to Mach number, temperature ratio, shear-layer thickness, and Reynolds number, the two simple jets considered here contain the main families of modes that exist for supersonic and subsonic jets over a wide range of operating conditions. The spatial spectra for the two jets at $St = 0.3$ and $m = 0$ are shown in figure 5. Other frequencies and azimuthal modes within our range of interest have qualitatively similar spectra. We have taken the liberty to omit from these plots a number of stable spurious modes which inevitably arise due to the dispersive nature of the finite-difference discretization used to approximate radial derivatives. Spurious modes can be distinguished from physical ones by the tendency of their eigenvalues to change significantly as the grid is refined and the prevalence of point-to-point oscillations in their eigenfunctions. We have also omitted stable convective modes to reduce clutter.

For supersonic jets, six families of modes can be distinguished and are denoted by color in figure 5(a). First, there is a single convectively unstable mode – the Kelvin-Helmholtz mode. Second, there are two continuous branches of vorticity and entropy modes that stably convect downstream at speeds ranging between the jet velocity and the co-flow velocity (omitted from plot). The third and fourth families are continuous branches of upstream and downstream free stream acoustic modes, which together radiate sound to all angles in the far-field. The fifth and sixth families are core pressure modes generated by resonant acoustic waves trapped within the potential core. These modes are discrete because of the confinement

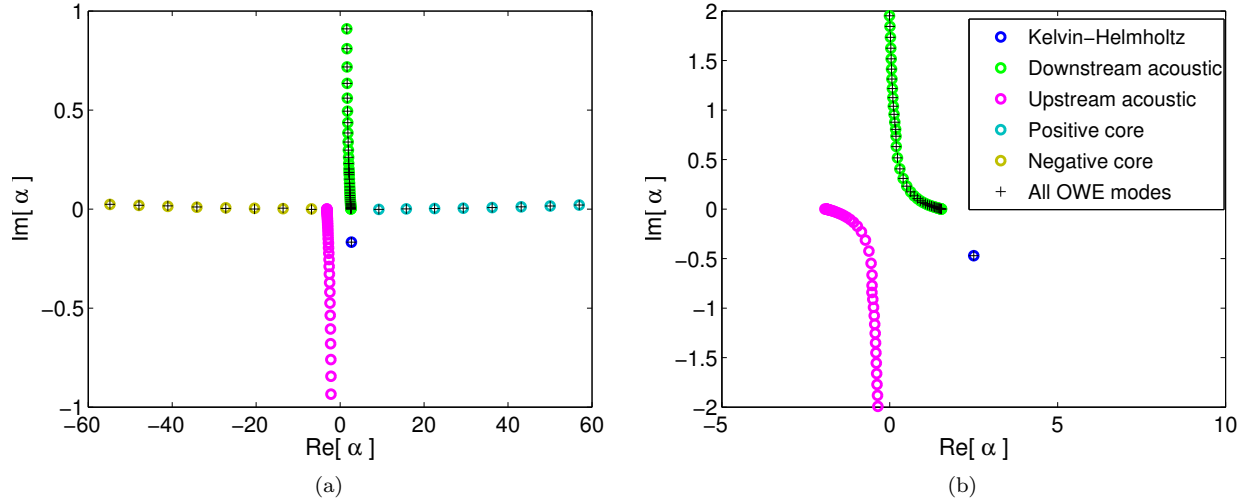


Figure 5: Spatial spectrum of the Euler equations for (a) supersonic jet, (b) subsonic jet. The legend identifies the different mode families and applies to both subplots. Note that the subsonic jet does not contain core modes. The spectrum of the one-way Euler operator for each jet is given by the black (+) symbols. In both cases, the upstream modes are properly removed, and all downstream modes are accurately represented.

caused by the shear layer. One of these families has positive phase velocity and one has negative phase velocity, but they both have positive group velocity because of the supersonic flow in the core, and so they are both downstream families of modes.³² This can be confirmed using Briggs' criterion.¹⁹

The spectrum of the Euler equations for the subsonic jet is shown in Figure 5(b). Four families of modes can be distinguished. The first two families are unchanged from the supersonic case: the discrete Kelvin-Helmholtz mode and the continuous convective vorticity and entropy branches (again omitted). The third and fourth families are the upstream and downstream acoustic branches. Since the flow is now subsonic everywhere, these branches contain only upstream and downstream propagating acoustic waves, respectively. No resonant core modes exist.

IV.A.2. One-way Euler spectrum

For the supersonic and subsonic jets, the b_+^j recursions parameters are divided evenly amongst the different families of downstream modes, and distributed over the regions over which each family is expected to appear. The locations of the acoustic branches and core modes can be predicted based on equation (37) with \bar{u}_x set to the free stream velocity and jet velocity, respectively. The locations of the Kelvin-Helmholtz mode and convective modes are estimates based on the range of possible convection velocities within the jet. Since there is only one upstream family in both jets, all of the b_-^j parameters are placed in the vicinity of the upstream free stream acoustic branch.

The (+) symbols in figure 5(a) are the eigenvalues of the one-way Euler operator with $N_b = 18$ for the supersonic jet. All downstream modes are accurately represented and the upstream free stream acoustic modes have been removed. Similarly, the (+) symbols in figure 5(b) show the eigenvalues of the one-way Euler operator with $N_b = 14$ for the subsonic jet. All downstream modes are accurately represented, and the upstream acoustic modes have been removed.

For use as a jet noise model, it is especially important that the one-way Euler equations accurately represent the low-angle free stream acoustic modes in both the supersonic and subsonic jets. Figure 6 concentrates on these low-angle acoustic modes and the Kelvin-Helmholtz mode and compares their one-way Euler and PSE representations. The PSE representation is based on the effective PSE spectrum, defined in Appendix B. Concisely, the effective PSE spectrum is the set of eigenvalues that, if exactly integrated, would produce the same results as PSE.

Recall that for PSE, the distortion of modes farther away from the Kelvin-Helmholtz mode is greater than

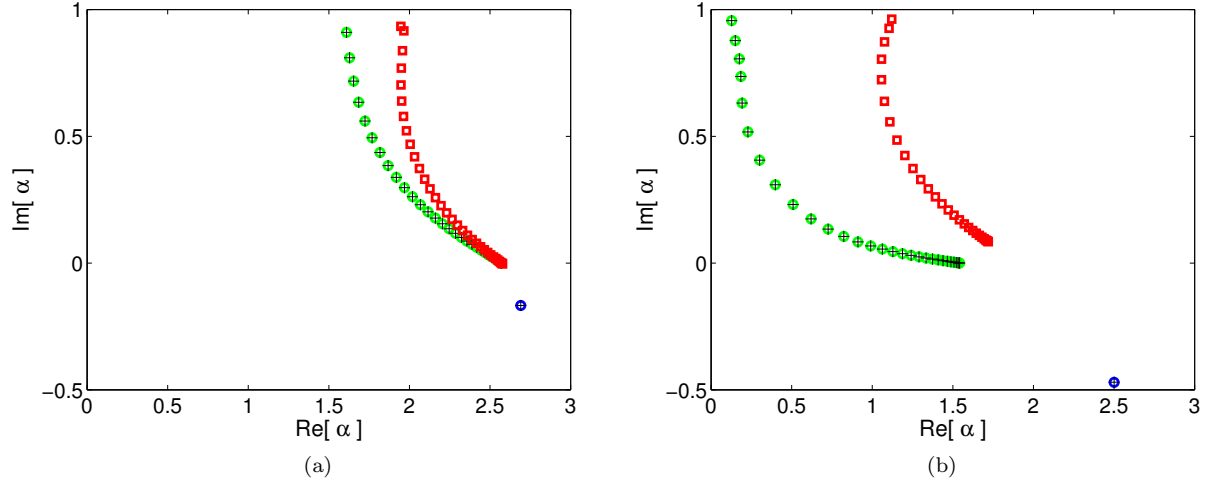


Figure 6: Comparison of the one-way Euler (+) and PSE (□) low angle acoustic modes to their full Euler counterparts (green ○) for the (a) supersonic and (b) subsonic jets. The one-way Euler modes are far more accurate than the PSE modes, especially for the subsonic jet. The location of the Kelvin-Helmholtz mode is also shown (blue ○).

for modes closer to it. For the supersonic jet, the relatively short distance between the Kelvin-Helmholtz mode and the low-angle acoustic modes allows PSE to retain them with reasonable accuracy. Still, the one-way Euler equations are much more accurate and represent the true eigenvalues almost perfectly. The main error in the PSE acoustic modes is an increase in wavelength (and therefore a reduction in phase speed), since the real parts of the eigenvalues move to higher values. There is, however, little excess damping. Since PSE already gives reasonable far-field sound predictions, it is unclear how much the improvement achieved in the spectrum of the one-way Euler operator will ultimately improve noise predictions for supersonic jets.

For the subsonic jet, the distance between the Kelvin-Helmholtz mode and the downstream acoustic modes is comparatively large. As a result, the PSE acoustic modes contain much more error. Their phase velocity is much too low and they are also significantly damped. The one-way Euler acoustic modes, on the other hand, are represented extremely accurately. This suggests that the one-way Euler method is capable of delivering greatly improved far-field noise predictions for subsonic jets, compared to PSE.

IV.B. Non-parallel subsonic jet

In this section, the one-way Euler method is applied to the mean flow of an experimentally measured turbulent subsonic jet. The jet has acoustic Mach number $M_\infty = \bar{u}_{jet}/\bar{c}_\infty = 0.5$, temperature ratio $\bar{T}_{jet}/\bar{T}_\infty = 0.96$, and Reynolds number $Re = 7 \times 10^5$. The axial velocity was measured using stereoscopic PIV in the Small Hot Jet Acoustic Rig at the NASA Glenn Research Center.³³ Velocity contours are shown in figure 7. Temperature is recovered using the Crocco-Busemann relation, and the radial velocity is estimated by enforcing continuity. The mean pressure and azimuthal velocity are constant and zero, respectively. To ensure reasonable smoothness of the baseflow, the mean axial velocity data is fit to radial and axial profiles similar to those used by previous investigators.^{3,11}

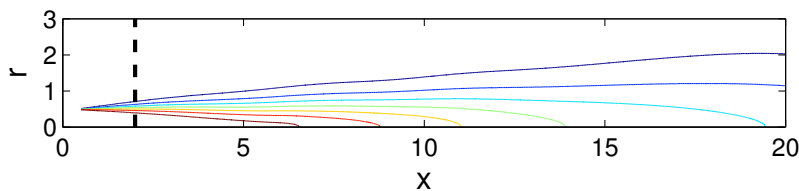


Figure 7: Axial velocity of the Mach 0.5 jet. The contours are evenly spaced between 0.1 and 0.99. The dashed line indicates the starting-point of for PSE and one-way Euler marches.

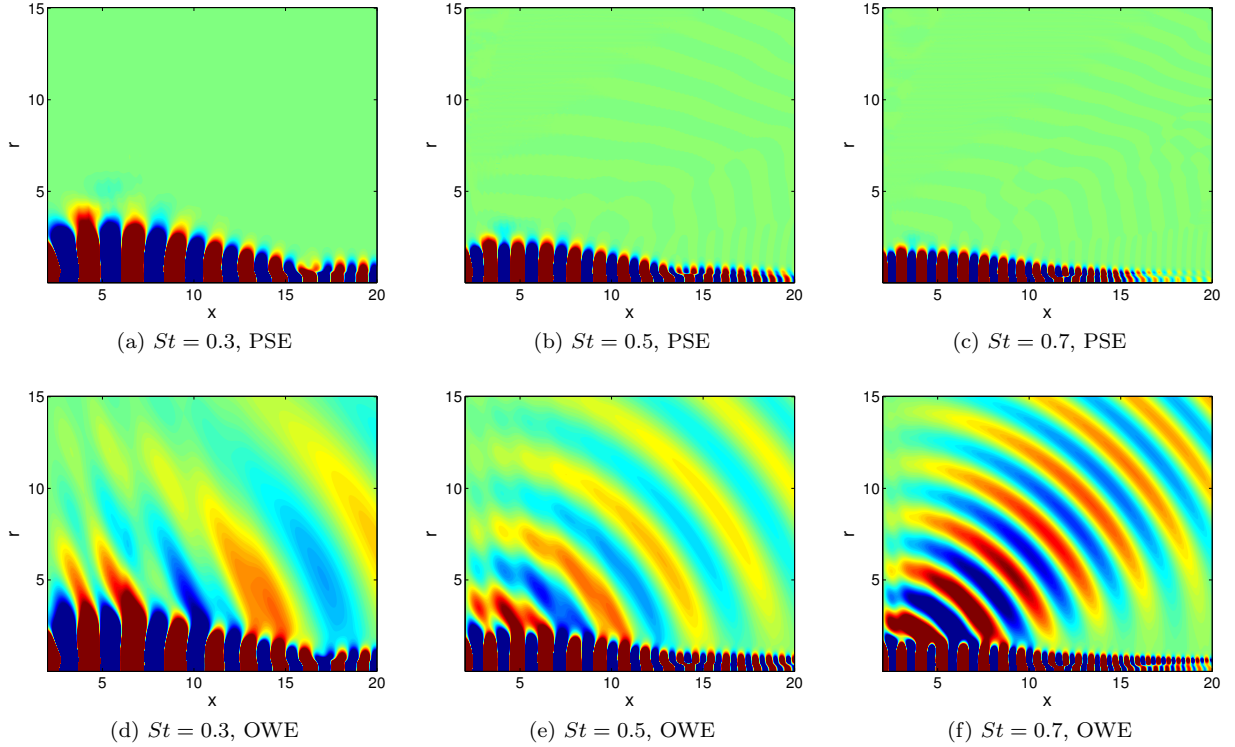


Figure 8: Pressure contours for the Mach 0.5 turbulent jet.

Gundmundsson & Colonius previously calculated modal solutions for this jet using PSE. They found good agreement between their results and POD filtered near-field microphone data, except at low Strouhal numbers for $m = 0$. Here, we compare results computed by PSE and the one-way Euler equations for $m = 0$ and $St = 0.3, 0.5, 0.7$. The domain extends fifteen jet diameters in the radial direction, and the equations are discretized as described in section III using approximately 800 grid points. A local Kelvin-Helmholtz eigenfunction is specified two diameters downstream of the nozzle and the solution is marched eighteen diameters downstream. We will discuss the effects of changing the position and form of the initial disturbance below. We use $N_b = 18$, and the recursion parameters are selected based on the strategy describes for the parallel subsonic jet.

Figure 8 shows the pressure field as computed by PSE and the one-way Euler equations. Both methods give similar near-field results, although the wavepacket decays slightly more rapidly in the PSE results, just as it did in the mixing layer test problem. The wavepacket along the lip-line at $St = 0.3$ is plotted in figure 9(a). As expected, the PSE results contain virtually no acoustic field. The one-way Euler results clearly do contain acoustic waves. The downstream acoustic field is qualitatively consistent with LEE solutions of similar jets (see for example, Baqui et al, 2013).³⁴ For instance, the angle of the strongest radiation increases with Strouhal number, and the pressure decays like $1/R$ away from the source region, where R is the distance along the direction of propagation. The pressure along $x = 15$ for $St = 0.3$ is shown in figure 9(b). PSE under-predicts the acoustic radiation by over four orders of magnitude.

Especially for the lower two Strouhal numbers, there exist some curious waveforms in the one-way Euler solutions at low x . The cause of the behavior is not yet known. We have verified that it is related neither to inadequate grid resolution nor radial boundary conditions. It also does not appear to be related to inadequate convergence of the one-way equations, as the solutions change very little in the range $12 < N_b < 24$. Instead, this behavior seems to be related to how and where the march is initiated. Changing these parameters effects the solutions, and especially these waveforms. Further investigation is need to strengthen this hypothesis and confirm that this behavior is not related to parabolization. While we do not believe that these particular waveforms are physical, it is actually a positive feature that the one-way equations are sensitive to the inlet conditions. With PSE, the specific form and location of the inlet conditions has minimal effect on the solution because everything except the Kelvin-Helmholtz mode is rapidly damped regardless of initial input. The

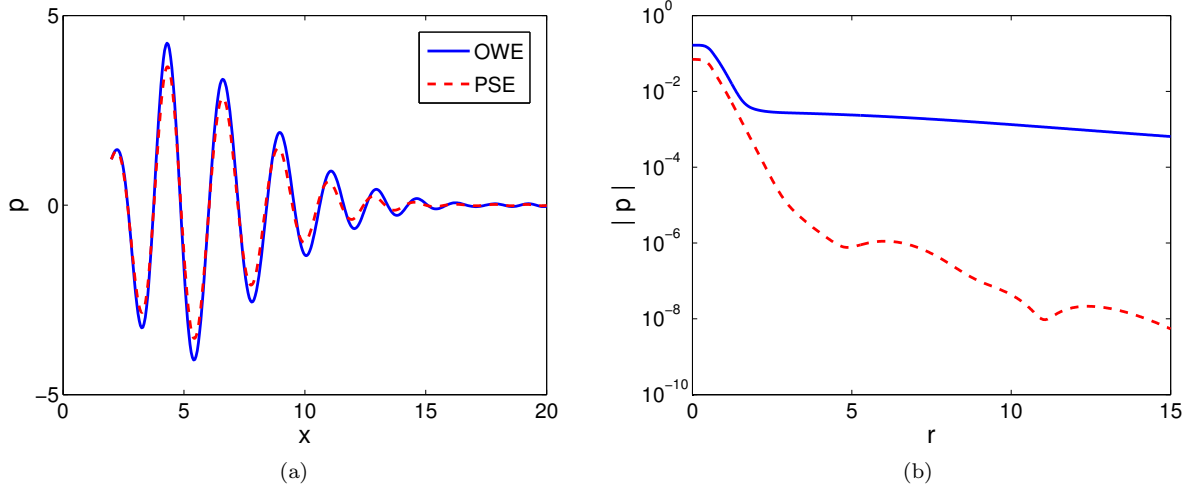


Figure 9: One-way Euler and PSE pressure results for $St = 0.3$, $m = 0$ at (a) $r = 1/2$, (b) $x = 15$.

development of large-scale structures in a real jet, on the other hand, is likely to be somewhat dependent on inlet disturbances. The increased sensitivity to inlet conditions of the one-way Euler results can therefore be leveraged to obtain an ensemble of solutions that can be analyzed and combined to obtain a more realistic aggregate result.

V. Summary and Future Work

In this paper, we have extended the one-way Euler method to cylindrical coordinates, verified its convergence, accuracy, and efficiency, and demonstrated its ability to properly parabolize the Euler equations for typical jet profiles. We then applied it for the first time to experimental mean flow data. The one-way Euler method eliminates the upstream acoustic modes from the Euler operator, resulting in a formally parabolic operator containing only downstream modes that can be stably and efficiently solved by spatial marching in the downstream direction. It is confirmed that for supersonic and subsonic parallel jets, the one-way Euler method properly retains all downstream propagating modes and successfully removes all upstream modes.

When applied to a Mach 0.5 turbulent jet based on experimental mean flow data, the one-way Euler equations produce similar near-field wavepackets as PSE, but unlike PSE also include the associated acoustic field. Basic properties of the one-way Euler acoustic field, such as far-field decay rate and directivity trends, match expectations, but the quantitative accuracy of these results still needs to be verified. The one-way Euler solutions also contain some irregular waveforms at low x that appear to be related to how and where the spatial march is initialized. This issue requires further investigation.

Overall, the results presented in this paper suggest that, with further development, the one-way Euler equations could be used to obtain improved accuracy over PSE as a low-cost jet noise model.

Appendices

A. Linearized Navier-Stokes operators

The linearized Navier-Stokes operators in specific volume, pressure form are:

$$A = \begin{bmatrix} \bar{u}_x & -\bar{\nu} & 0 & 0 & 0 \\ 0 & \bar{u}_x & 0 & 0 & \bar{\nu} \\ 0 & 0 & \bar{u}_x & 0 & 0 \\ 0 & 0 & 0 & \bar{u}_x & 0 \\ 0 & \gamma\bar{p} & 0 & 0 & \bar{u}_x \end{bmatrix}, \quad B_r = \begin{bmatrix} \bar{u}_r & 0 & -\bar{\nu} & 0 & 0 \\ 0 & \bar{u}_r - \frac{1}{Re} \frac{\bar{\nu}}{r} & 0 & 0 & 0 \\ 0 & 0 & \bar{u}_r - \frac{1}{Re} \frac{\bar{\nu}}{r} & 0 & \bar{\nu} \\ 0 & 0 & 0 & \bar{u}_r - \frac{1}{Re} \frac{\bar{\nu}}{r} & 0 \\ -\frac{\gamma}{RePr} \frac{\bar{p}}{r} & 0 & \gamma\bar{p} & 0 & \bar{u}_r - \frac{\gamma}{RePr} \frac{\bar{\nu}}{r} \end{bmatrix},$$

$$B_\theta = \frac{1}{r} \begin{bmatrix} \bar{u}_\theta & 0 & 0 & -\bar{\nu} & 0 \\ 0 & \bar{u}_\theta & 0 & 0 & 0 \\ 0 & 0 & \bar{u}_\theta & \frac{2}{Re} \frac{\bar{\nu}}{r^2} & 0 \\ 0 & 0 & -\frac{2}{Re} \frac{\bar{\nu}}{r^2} & \bar{u}_\theta & \bar{\nu} \\ 0 & 0 & 0 & \gamma\bar{p} & \bar{u}_\theta \end{bmatrix}, \quad B_{xx} = B_{rr} = r^2 B_{\theta\theta} = -\frac{1}{Re} \begin{bmatrix} 0 & 0 & 0 & 0 & 0 \\ 0 & \bar{\nu} & 0 & 0 & 0 \\ 0 & 0 & \bar{\nu} & 0 & 0 \\ 0 & 0 & 0 & \bar{\nu} & 0 \\ \frac{\gamma}{Pr} \bar{p} & 0 & 0 & 0 & \frac{\gamma}{Pr} \bar{\nu} \end{bmatrix},$$

$$L = \begin{bmatrix} -\nabla \cdot \bar{u} & \frac{\partial \bar{\nu}}{\partial x} & \frac{\partial \bar{\nu}}{\partial r} - \frac{\bar{\nu}}{r} & 0 & 0 \\ \frac{\partial \bar{p}}{\partial x} - \frac{1}{Re} \nabla^2 \bar{u}_x & \frac{\partial \bar{u}_x}{\partial x} & \frac{\partial \bar{u}_x}{\partial r} & 0 & 0 \\ \frac{\partial \bar{p}}{\partial r} - \frac{1}{Re} (\nabla^2 \bar{u}_r - \frac{\bar{u}_r}{r^2}) & \frac{\partial \bar{u}_r}{\partial x} & \frac{\partial \bar{u}_r}{\partial r} + \frac{1}{Re} \frac{\bar{\nu}}{r^2} & -\frac{2}{r} \bar{u}_\theta & 0 \\ -\frac{1}{Re} (\nabla^2 \bar{u}_\theta - \frac{\bar{u}_\theta}{r^2}) & \frac{\partial \bar{u}_\theta}{\partial x} & \frac{\partial \bar{u}_\theta}{\partial r} + \frac{\bar{u}_\theta}{r} & \frac{1}{r} \bar{u}_r + \frac{1}{Re} \frac{\bar{\nu}}{r^2} & 0 \\ -\frac{\gamma}{RePr} \nabla^2 \bar{p} & \frac{\partial \bar{p}}{\partial x} & \frac{\partial \bar{p}}{\partial y} & 0 & \gamma \nabla \cdot \bar{u} - \frac{\gamma}{RePr} \nabla^2 \bar{\nu} \end{bmatrix}.$$

The eigenvalues and diagonalizing transformation of the axial derivative matrix A are

$$\tilde{A} = \begin{bmatrix} \bar{u}_x & 0 & 0 & 0 & 0 \\ 0 & \bar{u}_x & 0 & 0 & 0 \\ 0 & 0 & \bar{u}_x & 0 & 0 \\ 0 & 0 & 0 & \bar{u}_x + \bar{c} & 0 \\ 0 & 0 & 0 & 0 & \bar{u}_x - \bar{c} \end{bmatrix}, \quad T = \begin{bmatrix} 1 & 0 & 0 & 0 & \bar{d}^2 \\ 0 & 0 & 1 & 0 & 0 \\ 0 & 0 & 0 & 1 & 0 \\ 0 & 1 & 0 & 0 & \bar{d} \\ 0 & -1 & 0 & 0 & \bar{d} \end{bmatrix},$$

where \bar{c} is the speed of sound and $\bar{d} = \frac{\bar{\nu}}{\bar{c}} = \frac{\bar{c}}{\gamma\bar{p}}$ is the acoustic admittance.

B. Effective PSE spectrum

The effective PSE spectrum is a tool for quantifying and visualizing the effects of PSE parabolization on the modes of the operator to which it is applied. We define the PSE spectrum as the set of eigenvalues that, if exactly integrated, would produce the same results as PSE. For a mode with eigenvalue $\imath\alpha$, PSE would advance the associated expansion coefficient as

$$\psi_{k+1} = \frac{1}{1 - \Delta x(\imath\alpha - \imath\alpha_0)} e^{\imath\alpha_0 \Delta x} \psi_k$$

where $\imath\alpha_0$ is the primary PSE mode – that is, the mode PSE is attempting to track. Now consider a different operator that supports the same eigenvector but with a different eigenvalue $\imath\alpha_{PSE}$. The *exact* advancement of this mode (assuming locally parallel flow) is given by

$$\psi_{k+1} = e^{\imath\alpha_{PSE} \Delta x} \psi_k$$

Equating these two solutions gives the effective PSE eigenvalue for this mode:

$$\imath\alpha_{PSE} = \imath\alpha_0 - \frac{1}{\Delta x} \log(1 - \Delta x(\imath\alpha - \imath\alpha_0))$$

As $\Delta x \rightarrow 0$, the correct eigenvalue $\iota\alpha$ is recovered, but this limit cannot be approached because of the PSE step-size restriction. At a fixed Δx , the distortion of each eigenvalue depends on its distance from the primary eigenvalue α_0 .

Acknowledgments

The authors gratefully acknowledge support from the Office of Naval Research under contract N0014-11-1-0753 with Dr. Brenda Henderson as technical monitor. Additionally, the authors would like to thank Professor Thomas Hagstrom, Southern Methodist University for helpful input on this work.

References

- ¹Jordan, P. and Colonius, T., “Wave Packets and Turbulent Jet Noise,” *Annual Review of Fluid Mechanics*, Vol. 45, 2013, pp. 173–195.
- ²Tam, C. K. W., Viswanathan, K., Ahuja, K. K., and Panda, J., “The sources of jet noise: experimental evidence,” *Journal of Fluid Mechanics*, Vol. 615, 11 2008, pp. 253–292.
- ³Tam, C. K. W. and Burton, D. E., “Sound generated by instability waves of supersonic flows. Part 2. Axisymmetric jets,” *J. Fluid Mech.*, Vol. 138, 1984, pp. 273–295.
- ⁴Suzuki, T. and Colonius, T., “Instability waves in a subsonic round jet detected using a near-field phased microphone array,” *Journal of Fluid Mechanics*, Vol. 565, 10 2006, pp. 197–226.
- ⁵Michalke, A., “An Expansion Scheme for the Noise from Circular Jets,” *Z. Flugwiss*, Vol. 19, 1971.
- ⁶Mattingly, G. E. and Chang, C. C., “Unstable waves on an axisymmetric jet column,” *Journal of Fluid Mechanics*, Vol. 65, 9 1974, pp. 541–560.
- ⁷Crighton, D. G. and Gaster, M., “Stability of slowly diverging jet flow,” *Journal of Fluid Mechanics*, Vol. 77, 1976, pp. 397–413.
- ⁸Tam, C. K. W. and Morris, P. J., “The radiation of sound by the instability waves of a compressible plane turbulent shear layer,” *Journal of Fluid Mechanics*, Vol. 98, 5 1980, pp. 349–381.
- ⁹Herbert, T., “Parabolized stability equations,” *Annu. Rev. Fluid Mech.*, Vol. 29, 1997, pp. 245–283.
- ¹⁰Colonius, T., Samanta, A., and Gudmundsson, K., “Parabolized stability equation models of large-scale jet mixing noise,” *IUTAM Symposium on Computational Aero-Acoustics for Aircraft Noise Prediction*, Southampton, UK, March, 2010.
- ¹¹Gudmundsson, K. and Colonius, T., “Instability wave models for the near-filed fluctuations of turbulent jets,” *J. Fluid Mech.*, Vol. 689, 2011, pp. 97–128.
- ¹²Rodriguez, D., Sinha, A., Brs, G. A., and Colonius, T., “Acoustic field associated with parabolized stability equation models in turbulent jets,” *19th AIAA/CEAS Aeroacoustics Conference, AIAA Paper 2013-2279*, Berlin, Germany, May 2013.
- ¹³Cheung, L. and Lele, S., “Aeroacoustic noise prediction and the dynamics of shear layers and jets using the nonlinear parabolized stability equations,” Tech. Rep. TF-103, 2007.
- ¹⁴Li, F. and Malik, R., “Spectral analysis of the parabolized stability equations,” *Computers & Fluids*, Vol. 26, No. 3, 1997, pp. 279–297.
- ¹⁵Li, F. and Malik, M., “On the Nature of PSE Approximation,” *Theoret. Comput. Fluid Dynamics*, Vol. 8, 1996, pp. 253–273.
- ¹⁶Andersson, P., Henningson, D., and Hanifi, A., “On a stabilization procedure for the parabolic stability equations,” *J. Engr. Mech.*, Vol. 33, 1998, pp. 311–332.
- ¹⁷Towne, A. and Colonius, T., “Improved Parabolization of the Euler Equations,” *19th AIAA/CEAS Aeroacoustics Conference, AIAA Paper 2013-2171*, Berlin, Germany, May 2013.
- ¹⁸Rubin, S. and Tannehill, J., “Parabolized/Reduced Navier-Stokes computational techniques,” *Annu. Rev. Fluid Mech.*, Vol. 24, 1992, pp. 117–144.
- ¹⁹Briggs, R. J., *Electron-Stream Interactions with Plasmas*, MIT Press, Cambridge, Massachusetts, 1964.
- ²⁰Kreiss, H., “Initial Boundary Value Problems for Hyperbolic Systems,” *Commun. Pure Appl. Math*, Vol. 23, 1970, pp. 277–298.
- ²¹Givoli, D. and Neta, B., “High-order nonreflecting boundary scheme for time- dependent waves,” *J. Comput. Phys.*, Vol. 186, 2003, pp. 24–46.
- ²²Hagstrom, T. and Warburton, T., “A new auxiliary variable formulation of high-order local radiation boundary conditions: corner compatibility conditions and extensions to first-order systems,” *Wave Motion*, Vol. 39, 2004, pp. 890–901.
- ²³Hagstrom, T., *Topics in Computational Wave Propagation, vol.31 of Lecture Notes in Computational Science and Engineering*, Vol. 70, chap. New results on absorbing layers and radiation boundary conditions, Springer-Verlag, New York, 2003, pp. 1–42.
- ²⁴Mattsson, K. and Nordstrm, J., “Summation by parts operators for finite difference approximations of second derivatives,” *Journal of Computational Physics*, Vol. 199, No. 2, 2004, pp. 503 – 540.
- ²⁵Colonius, T. and Ran, H., “A super-grid-scale model for simulating compressible flow on unbounded domains,” *J. Comput. Phys.*, Vol. 182, No. 1, 2002, pp. 191–212.
- ²⁶Appelo, D. and Colonius, T., “A high-order super-grid-scale absorbing layer and its application to linear hyperbolic systems,” *J. Comput. Phys.*, Vol. 228, No. 11, 2009, pp. 4200–4217.
- ²⁷Thompson, K. W., “Time Dependent Boundary Conditions for Hyperbolic Systems,” *J. Comput.l Phys.*, Vol. 68, 1987, pp. 1–24.

- ²⁸Mohseni, K. and Colonius, T., “Numerical treatment of polar coordinate singularities,” *J. Comput. Phys.*, Vol. 157, No. 2, Jan. 2000, pp. 787–795.
- ²⁹Yule, A., “Two-Dimensional Self-Preserving Turbulent Mixing Layers at Different Free Stream Velocity Ratios,” Tech. rep., University of Manchester, 1972.
- ³⁰Morris, P. J., “The spatial viscous instability of axisymmetric jets,” *Journal of Fluid Mechanics*, Vol. 77, 10 1976, pp. 511–529.
- ³¹Michalke, A., “Survey on jet instability theory,” *Progress in Aerospace Sciences*, Vol. 21, No. 0, 1984, pp. 159 – 199.
- ³²Tam, C. K. W. and Hu, F. Q., “On the three families of instability waves of high-speed jets,” *Journal of Fluid Mechanics*, Vol. 201, 4 1989, pp. 447–483.
- ³³Bridges, J. and Wernet, M., “Measurements of the aeroacoustic sound sources in hot jets,” *AIAA Paper 2003-3130*, 2003.
- ³⁴Baqui, Y. B., Agarwal, A., Cavalieri, A., and Sinayoko, S., “Nonlinear and linear noise source mechanisms in subsonic jets,” *19th AIAA/CEAS Aeroacoustics Conference, AIAA Paper 2013-2279*, Berlin, Germany, May 2013.